Correction of non-linearities in quadrature phase differential interferometry

Dandara Velasco, Caroline Cramail, Jérôme Giraud, Benjamin Cross, Romain Lhermerout

Correction of non-linearities in quadrature phase differential interferometry

Dandara Velasco Anez, Caroline Cramail, Jérôme Giraud, Benjamin Cross and Romain Lhermerout

Univ. Grenoble Alpes, CNRS, LIPhy, 38000 Grenoble, France

E-mail: romain.lhermerout@univ-grenoble-alpes.fr

September 2024

Abstract. Quadrature phase differential interferometry is a technique of choice for measuring arbitrary large displacements with record resolution. The so-called Heydemann corrections are generally employed to take account of the unavoidable imperfections due to the optics or the electronics, and a linearisation of the signals is usually performed when the displacement to be determined is the superposition of a quasi-static component and a small harmonic component. Here we show that this standard analysis can lead to non-linearities of two types. The first type of non-linearities is due to optical and electronic imperfections that were not reported in the past and not included in the Heydemann corrections. These imperfections appear as amplitude difference and phase shift between each pair of intensity signals, and produce periodic non-linearities of nanometer amplitude when the intensity signals are combined to obtain contrats, i.e., quantities that are insensitive to intensity fluctuations of the light source. The second type of non-linearities is due to large amplitudes of harmonic oscillation, which become significant when the oscillations are typically larger than 20 nm for a red-emitting laser source, and can lead to an underestimation of the measured amplitude of ~ 20 %. In order to correct these non-linearities, new procedures of calibration and analysis are presented, implemented and successfully tested over a wide range of quasi-static velocities, frequencies and amplitudes of harmonic oscillation. The proposed corrections reduce non-linearities below the noise level, making them smaller than 100 pm and 10 pm for the quasi-static and harmonic displacement, respectively.

Keywords: interferometry, non-linearities, Heydemann corrections

Submitted to: *Meas. Sci. Technol.*

1. Introduction

Differential interferometry is a technique of choice to measure extremely small displacements. The initial design, imagined by Nomarsky in 1955 [1, 2], has proved to offer an exquisite sensitivity, only limited by the shot noise inherent to photodetectors [3]. A key factor for such outstanding performances is that the interfering beams are spatially separated over small distances, limiting the impact of environmental perturbations. An improved design was proposed by Bellon *et al.* in 2002 [4], which consists in adding an arm in the optical set-up to measure not only the cosine but also the sine of the phase to be determined. This so-called quadrature phase interferometric technique applied to differential interferometry allows to measure very large displacements with a constant, maximum, sensitivity.

Quadrature phase differential interferometry can be seen as single-pixel holographic interferometry. While the purpose of holographic techniques [5, 6, 7] is to obtain interference patterns through which the 3D shape or deformation field of an object can be resolved, we focus here on the displacement of a single mirror relative to a reference mirror. Optical phase unwrapping is an essential and delicate problem for holographic techniques [8, 9]. In the case of quadrature phase differential interferometry, the interference pattern presents no fringes, as in the central zone of a Michelson interferometer at optical contact. The optical phase is deduced from the intensity level of the light, and can be easily unwrapped by following its evolution over time.

Quadrature phase differential interferometry has been applied in the context of force measurements, first with the Atomic Force Microscope (AFM) [3], then with the dynamic Surface Force Apparatus (dSFA) in our team [10]. In the dSFA case, the phase to be determined is the sum of a quasi-static component and of a small harmonic component, leading to a linear analysis considering the harmonic component as a perturbation of the static one. It is evident that such interferometry should provide quantitative measurements to access delicate physical quantities as nanometric hydrodynamic slip length [11], to name but one example. This is why calibrations of the dual output are performed to take account of the unavoidable imperfections due to the optics or the electronics, generally using the corrections proposed by Heydemann in 1981 [12] in the general context of quadrature phase interferometry. In short, Heydemann corrections take into account the fact that the dual outputs are not perfectly equal to the cosine and the sine of the phase to be measured, but have different offsets, amplitudes and phase shifts.

In the present article, we show that the Heydemann corrections and the linear treatment of the harmonic perturbation are not sufficient, leading to non-linearities of two types:

- non-linearities due to optical and electronic imperfections, appearing when combining the different signals to obtain normalized quantities which are insensitive to any intensity fluctuations of the light source,
- non-linearities due to large amplitudes of harmonic oscillation, for which the linearisation of the interferometric signals (as a quasi-static component plus a single harmonic component) is no longer valid.

After highlighting these non-linearities, we propose and implement a general method to correct them.

The manuscript is organized as follows: in section 2 we describe the experimental set-up, in section 3 we present the key ideas of the analysis in the case of ideal signals, in sections 4 and 5 we explain the methods to correct the two types of non-linearities, in section 6 we test the robustness of these corrections and in section 7 we discuss these findings in relation to literature.

2. Experimental setup

Optics. The optical interferometer, sketched in Figure 1, is composed of three areas.

In the "Beam preparation" area, a stabilized He-Ne laser (SIOS SL 04/A) produces a linearly-polarized beam ($\lambda = 632.9912 \pm 0.0002$ nm) oriented at 0°. A Faraday isolator (Thorlabs IO-3D-633-PBS) rotates the direction of polarization by 45° and prevents any reflected light from re-entering the laser cavity and destabilizing its emission. A Glan-Taylor polarizer with a 100 000:1 extinction ratio (Thorlas GT10-A) oriented at 45° ensures the quality of the beam's polarization, and a convergent lens (Thorlabs LA1908-A) allows to focus the beam on the photodetectors (described after).

In the "Sensing" area, the beam passes through a first 50:50 non-polarizing beamsplitter (Thorlabs BS013), and half of its intensity is directed towards a calcite crystal (Thorlabs BD40) oriented at 0°. The incident beam is linearly polarised at 45° with the principal axis of the calcite, and is therefore spatially separated in two parallel beams of equal intensities and orthogonal linear polarizations. The two beams are reflected by two mirrors (Fichou, aluminium-coated BK7), which are parallel and shifted by a distance H to be determined. After reflection the beams are spatially recombined by the calcite and again passes through the first beamsplitter, forming a beam of elliptical polarization, due to the phase shift between the two orthogonal components of the polarization, equal to:

$$\phi = \frac{4\pi H}{\lambda}, \tag{1}$$

where the factor 2 is due to the back and forth trajectories of the beams.

In the "Analysis" area, the beam passes through a second identical beamsplitter. Half of the light goes in the "X arm", composed of a Wollaston prism (Thorlabs WP10-A) oriented at 45° with the principal axis of the calcite, which projects the two orthogonal components of the polarization onto the ±45° axis and therefore make them interfere. Two separated beams emerge from the Wollaston prism, and their intensities are measured with two photodiodes (Osram Opto Semiconductors, SFH 206 K), giving the photocurrents $I^{\mathrm{X1}} = \frac{I_0}{2}(1+\cos\phi)$ and $I^{\mathrm{X2}} = \frac{I_0}{2}(1-\cos\phi)$, with I_0 corresponding to the incident intensity (in the ideal case, see after). The other half of the light emerging from the second beamsplitter goes in the "Y arm", which is similar to the X arm except that a quarter-wave plate (Lambda Research Optics WPZM-25.4-20.0CQ-0) oriented at 0° has been inserted before the Wollaston prism. This is the quadrature phase technique, which allows to measure the photocurrents $I^{\mathrm{Y1}} = \frac{I_0}{2}(1+\sin\phi)$ and $I^{\mathrm{Y2}} = \frac{I_0}{2}(1-\sin\phi)$. Finally, a general expression for the four photocurrents can be written as:

$$I^{\mathrm{X1}}_{\mathrm{Y2}} = \frac{I_0}{2}\left(1 \pm \begin{matrix}\cos\\ \sin\end{matrix}\phi\right), \tag{2}$$

where the + or − sign refers to the photodiode 1 or 2, and the cos or sin function refers to the X or Y arm, respectively. The measured photocurrents can then be analysed to deduce the phase shift ϕ via equation 2 and the distance H via equation 1.

Electro-mechanics. One mirror is actuated while the other is fixed, in such a way that the distance between them is controlled over time t as:

$$H = H_{\mathrm{stat}} + H_{\mathrm{dyn}}\cos(\omega t + \varphi). \tag{3}$$

The left-hand term is a (quasi-)static component varying at constant velocity as $H_{\mathrm{stat}} = vt$, with $|v|$ typically chosen between 0.1 nm/s and 100 nm/s, over a total range of about 1 μm. The right-hand side term is a dynamic component of sinusoidal shape, with an amplitude $H_{\mathrm{dyn}} > 0$ typically chosen between 0.7 nm and 70 nm and a frequency $\omega/(2\pi)$ between 10 Hz and 500 Hz. Combining equations 1 and 3, the phase shift therefore reads:

$$\phi = \phi_{\mathrm{stat}} + \phi_{\mathrm{dyn}}\cos(\omega t + \varphi), \tag{4}$$

with $\phi_{\mathrm{stat}} = \frac{4\pi H_{\mathrm{stat}}}{\lambda}$ and $\phi_{\mathrm{dyn}} = \frac{4\pi H_{\mathrm{dyn}}}{\lambda} > 0$. In the present study, i.e., for the application of this interferometry technique to dSFA, we want to simultaneously determine the quasi-static and harmonic displacements from the measured photocurrents. In this regard, the situation is very different from modulation techniques in which a known harmonic displacement is applied in order to measure only the quasi-static displacement (as for example in [13]).

The home-made actuator used in this study has been described in details elsewhere [10]. In short, it is first composed of a flexure hinge, which geometry ensures a deflection in an almost perfectly straight motion: a residual rotation of 0.5 prad for 1 μm of translation [14] (the maximum range used), i.e., almost 7 orders of magnitude smaller than the laser beam drift. Its second component is a coil-magnet system which permits a fine control of the force applied to the flexure hinge. The two ends of the coil are connected to the output of a function generator (Keysight 33220A) providing a quasi-static saw-shape voltage of desired slope, and to the output of a lock-in amplifier (Stanford Research System SR830) providing a dynamic voltage of sinusoidal shape and amplitude V_{dyn}. When all these components are operated in conditions where they respond linearly, which is the case for displacements smaller than 1 μm, this actuator allows to precisely control the distance as shown in equation 3, in particular with a constant velocity over the entire displacement range.

Opto-electronics. The photodiodes are operated in photovoltaic mode, to avoid dark current and to ensure low noise and best linearity, at a modest price in terms of dynamics given the frequencies used.

Each photodiode corresponding to the signals I^{X1} and I^{Y1} is connected in series with two amperemeters. The first one is a precision multimeter (Keysight 34465A) working in DC current mode to measure the static component of the photo-current, with a 1-day precision of $\sim$ 1 nA for a 10 μA range. The second one is a lock-in amplifier (Stanford Research System SR830) working in current mode to measure the modulus and phase of the harmonic component of the photo-current, with resolutions of respectively 100 pA

and 0.01°. In the case of the signals I^{X2} and I^{Y2}, each photodiode is connected only to a a precision multimeter.

The signals measured by the four precision multimeters and the two lock-in amplifiers are acquired simultaneously by TTL triggering every $T = 1$ s, with an integration time $\tau = 0.1$ s.

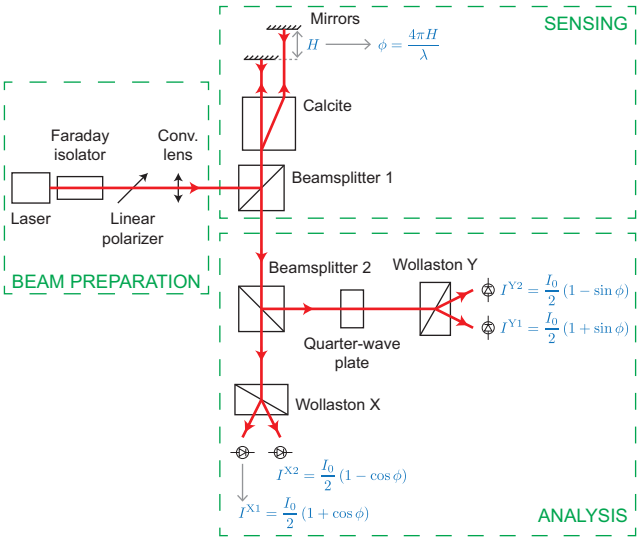

Figure 1. Schematic of the optical interferometer.

3. Analysis in the case of ideal signals

Conditions. The analysis of the measurements obtained with quadrature phase differential interferometry applied to the dSFA is based on four general conditions. These conditions are stated in this subsection, and their importance will be shown in the next subsection.

The first one is a linearity condition. For the photocurrents (equation 2) to be linearized as a static plus a single harmonic component, one has to verify:

$$\frac{4\pi H_{\rm dyn}}{\lambda} \ll 1 \quad \Leftrightarrow \quad H_{\rm dyn} \ll \frac{\lambda}{4\pi} \sim 50 \text{ nm}. \tag{5}$$

The second one is a quasi-static condition, i.e., the quasi-static component of the distance has to vary slowly enough to be considered as a constant at the timescale of the integration time:

$$\frac{4\pi|v|\tau}{\lambda} \ll 1 \quad \Leftrightarrow \quad |v| \ll \frac{\lambda}{4\pi\tau} \sim 500 \text{ nm/s}. \tag{6}$$

The third one is a sampling condition, i.e., the quasi-static component of the distance has to vary slowly enough for the interferogram to be followed at the timescale of the acquisition period:

$$\frac{4\pi|v|T}{\lambda} \ll 1 \quad \Leftrightarrow \quad |v| \ll \frac{\lambda}{4\pi T} \sim 50 \text{ nm/s}. \tag{7}$$

The fourth one can be termed as a filtering condition, and should be verified for the precision multimeters to measure only the static component, and the lock-in amplifiers to measure only the harmonic component at the working frequency $\omega/(2\pi)$. One can show that this condition is:

$$\frac{\omega\tau}{2} \gg 1 \quad \Leftrightarrow \quad \frac{\omega}{2\pi} \gg \frac{1}{\pi\tau} \sim 3 \text{ Hz}. \tag{8}$$

Photocurrents. Under the aforementioned conditions and in the case of ideal signals (we will specify what it means in the next sections), the measured photocurrents have simple analytical expressions. In the following, we will consider only channel X1, as analogous expressions can be found for the other channels. Thanks to the linearity condition (equation 5), the photocurrent can be expanded at first order in $\phi_{\rm dyn}$:

$$I^{X1} \simeq \frac{I_0}{2}\left[1 + \cos\phi_{\rm stat} - \sin\phi_{\rm stat} \times \phi_{\rm dyn}\cos(\omega t + \varphi)\right]. \tag{9}$$

The precision multimeter collects the static component (i.e., the component at zero frequency) by integrating the signals over τ at a time t:

$$I^{X1}_{\rm stat}(t) \equiv \int_t^{t+\tau} I^{X1}(t')\frac{dt'}{\tau}. \tag{10}$$

The quasi-static condition (equation 6) allows to consider $\phi_{\rm stat}$ as a constant over the integration time τ, and the temporal integration of equation 9 provides:

$$I^{X1}_{\rm stat}(t) \simeq \frac{I_0}{2}\Big[1 + \cos\phi_{\rm stat} - \sin\phi_{\rm stat} \times \phi_{\rm dyn}\cos\left(\omega t + \varphi + \frac{\tau}{2}\right)\text{sinc}\left(\frac{\omega\tau}{2}\right)\Big], \tag{11}$$

Thanks to the filtering condition (equation 8), the cardinal function sinc is close to zero and we finally obtain:

$$I^{X1}_{\rm stat}(t) \simeq \frac{I_0}{2}\left(1 + \cos\phi_{\rm stat}\right). \tag{12}$$

Note that the sampling condition (equation 7) ensures that the acquisition rate is sufficient to be able to follow the quasi-static evolution of the interferogram.

The lock-in amplifier collects the two RMS quadratures of the harmonic component (real and imaginary parts) at the working frequency $\omega/(2\pi)$. It can formally be written as:

$$I_{\rm re}^{\rm X1}(t) \equiv \int_{t}^{t+\tau} I^{\rm X1}(t^{'})\sqrt{2}\cos(\omega t)\frac{dt^{'}}{\tau} \tag{13}$$

$$I_{\rm im}^{\rm X1}(t) \equiv \int_{t}^{t+\tau} I^{\rm X1}(t^{'})\sqrt{2}\cos\left(\omega t+\frac{\pi}{2}\right)\frac{dt^{'}}{\tau}. \tag{14}$$

In the same way as for the static components and under the same conditions, one can show that these quantities are equal to:

$$I_{\rm re}^{\rm X1}(t) \simeq -\frac{I_0}{2\sqrt{2}}\sin\phi_{\rm stat}\times\phi_{\rm dyn}\cos\varphi \tag{15}$$

$$I_{\rm im}^{\rm X1}(t) \simeq -\frac{I_0}{2\sqrt{2}}\sin\phi_{\rm stat}\times\phi_{\rm dyn}\sin\varphi. \tag{16}$$

Equivalently, it can be expressed with the modulus and argument of the harmonic component:

$$I_{\rm mod}^{\rm X1}(t) \simeq \frac{I_0}{2\sqrt{2}}\left|\sin\phi_{\rm stat}\right|\phi_{\rm dyn} \tag{17}$$

$$I_{\rm arg}^{\rm X1}(t) \simeq \varphi \text{ if } \sin\phi_{\rm stat}<0,\ \varphi+\pi \text{ otherwise.} \tag{18}$$

Contrasts. In order to obtain normalized quantities which are insensitive to any intensity fluctuations of the light source, we numerically combine the measurements from each pair of photodiodes to compute contrasts. We define static contrasts as:

$$C_{\rm stat}^{\rm X} \equiv \frac{I_{\rm stat}^{\rm X1}-I_{\rm stat}^{\rm X2}}{I_{\rm stat}^{\rm X1}+I_{\rm stat}^{\rm X2}} \simeq \cos\phi_{\rm stat} \tag{19}$$

$$C_{\rm stat}^{\rm Y} \equiv \frac{I_{\rm stat}^{\rm Y1}-I_{\rm stat}^{\rm Y2}}{I_{\rm stat}^{\rm Y1}+I_{\rm stat}^{\rm Y2}} \simeq \sin\phi_{\rm stat}. \tag{20}$$

We define dynamic contrasts in a consistent way as:

$$C_{\rm mod}^{\rm X} \equiv 2\sqrt{2}\frac{I_{\rm mod}^{\rm X1}}{I_{\rm stat}^{\rm X1}+I_{\rm stat}^{\rm X2}} \simeq \left|\sin\phi_{\rm stat}\right|\phi_{\rm dyn} \tag{21}$$

$$C_{\rm mod}^{\rm Y} \equiv 2\sqrt{2}\frac{I_{\rm mod}^{\rm Y1}}{I_{\rm stat}^{\rm Y1}+I_{\rm stat}^{\rm Y2}} \simeq \left|\cos\phi_{\rm stat}\right|\phi_{\rm dyn} \tag{22}$$

$$C_{\rm arg}^{\rm X} \equiv I_{\rm arg}^{\rm X1},\ {\rm C}_{\rm arg}^{\rm Y} \equiv {\rm I}_{\rm arg}^{\rm Y1}. \tag{23}$$

Note that moduli here are not RMS values.

Displacements. The static displacement $H_{\rm stat}$ can deduced from the static contrasts:

$$H_{\rm stat} = \frac{\lambda}{4\pi}\arctan\left(\frac{{\rm C}_{\rm stat}^{\rm Y}}{{\rm C}_{\rm stat}^{\rm X}}\right)\ \left(\bmod\ \frac{\lambda}{2}\right). \tag{24}$$

Thanks to the quadrature, this is performed with a sensitivity which is independent of the value of $H_{\rm stat}$. The static displacement is initially determined modulo $\frac{\lambda}{2}$, but then the signal can be unwrapped over time, providing that the interferogram varies slowly enough (sampling condition given by equation 7). As we have no way to detect the optical contact (corresponding to zero phase shift), the static displacement is finally known to within one constant.

The harmonic displacement $H_{\rm dyn}$ is obtained by numerically combining the different contrasts as:

$$x \equiv -C_{\rm mod}^{\rm X}\cos\left(C_{\rm arg}^{\rm X}\right)C_{\rm stat}^{\rm Y}+C_{\rm mod}^{\rm Y}\cos\left(C_{\rm arg}^{\rm Y}\right)C_{\rm stat}^{\rm X} \tag{25}$$

$$y \equiv -C_{\rm mod}^{\rm X}\sin\left(C_{\rm arg}^{\rm X}\right)C_{\rm stat}^{\rm Y}+C_{\rm mod}^{\rm Y}\sin\left(C_{\rm arg}^{\rm Y}\right)C_{\rm stat}^{\rm X} \tag{26}$$

$$H_{\rm dyn} = \frac{\lambda}{4\pi}\sqrt{x^2+y^2}. \tag{27}$$

This is achieved with a sensitivity which is independent of the working point, i.e., independent of the value of $H_{\rm stat}$.

4. Correction of non-linearities due to optical and electronic imperfections

Imperfections. Experimentally, we observe that the photocurrents differ slightly from equation 2. For example we have for channel X1:

$$I^{\rm X1} = a^{\rm X1}\ \frac{I_0}{2}\left[1+b^{\rm X1}\cos\left(\phi+\psi^{\rm X1}\right)\right], \tag{28}$$

with $a^{\rm X1}$ and $b^{\rm X1}$ which are close but less than 1, and $\psi^{\rm X1}$ which is close but different from 0. Similar equations can be written for the other three channels, with different factors a^i, b^i and ψ^i. Note that the additional phase shift $\psi^{\rm X1}$ cannot simply be included in the phase shift ϕ (which will be determined to within one constant anyway), because it is not the same on the different channels ($\psi^{\rm X1}\neq\psi^{\rm X2}\neq\psi^{\rm Y1}\neq\psi^{\rm Y2}$).

Some of these imperfections were already pointed out in the seminal paper of Heydemann [12]. He considered only the raw signals (i.e., photocurrents and not contrasts, in the terminology of the present paper) and the effects of $a^{\rm X1}\neq a^{\rm Y1}$, $b^{\rm X1}\neq b^{\rm Y1}$ and $\psi^{\rm X1}\neq\psi^{\rm Y1}$. These factors may have various origins in our set-up, which can be listed in a non-exhaustive way. The factors $a^{\rm X1}\neq a^{\rm Y1}$ and $b^{\rm X1}\neq b^{\rm Y1}$ are caused by imperfect beams superposition, beams clipping, and slightly different adsorption coefficients and photodiodes sensitivities. The factors $b^{\rm X1}\neq b^{\rm Y1}$ can be further reduced by an imperfect inclination of the Wollaston prisms in the plane perpendicular to the propagation. The factors $\psi^{\rm X1}\neq\psi^{\rm Y1}$ are induced by an imperfect orientation of the quarter-wave plate, and

by optical elements like beamsplitters which are not perfectly non-polarizing.

In the present study, we consider normalized signals in order to be insensitive to any intensity fluctuations of the laser; therefore we make use of the channels labelled as "2". We find significant differences between the photocurrents coming from each pair of photodiodes, i.e., $a^{\mathrm{X1}} \neq a^{\mathrm{X2}}$, $b^{\mathrm{X1}} \neq b^{\mathrm{X2}}$ and $\psi^{\mathrm{X1}} \neq \psi^{\mathrm{X2}}$. These discrepancies can be observed and precisely calibrated by performing a "calibration actuation", which consists in applying a quasi-static displacement at constant velocity $v = 2.45$ nm/s (slow enough to fulfil the quasi-static and sampling conditions, fast enough to have little influence of drifts) over a range of ~ 1 μm (to cover ~ 2 periods of static phase) and a harmonic voltage of frequency $\omega/(2\pi) = 30$ Hz (large enough to fulfil the filtering condition, small enough to have the maximum response of the flexure hinge) and of amplitude $V_{\mathrm{dyn}} = 0.01$ $\mathrm{V_{rms}}$, corresponding to oscillations of amplitude ~ 1.8 nm (small enough to fulfil the linearity condition, large enough to have little influence of noise) to the actuator. In Figure 2(a) are plotted the temporal evolutions of $I^{\mathrm{X1}}_{\mathrm{stat}}$ (in red) and $I^{\mathrm{X2}}_{\mathrm{stat}}$ (in blue), together with sinusoidal fits of common frequency f_{calib} (in green). Even if, at first glance, the signals look like identical sinusoids in antiphase, the fits show that the offsets differ by $\sim 2.2\%$, the amplitudes differ by $\sim 0.13\%$ and that there is a phase shift of $(\pi+) \sim 0.048$ rad between them. These differences are not due to fitting errors or random noise, as shown by numerically computing the "simple sum":

$$\mathrm{sum}\left[I^{\mathrm{X1,X2}}_{\mathrm{stat}}\right] \equiv I^{\mathrm{X1}}_{\mathrm{stat}} + I^{\mathrm{X2}}_{\mathrm{stat}}. \tag{29}$$

This quantity is represented in red in Figure 2(b), and exhibits residual oscillations at frequency f_{calib}, while sinusoidal signals of exact same amplitude and in perfect antiphase would lead to a constant signal. The factors $a^{\mathrm{X1}} \neq a^{\mathrm{X2}}$ and $b^{\mathrm{X1}} \neq b^{\mathrm{X2}}$ may have various origins among the ones mentioned previously, whereas the factors $\psi^{\mathrm{X1}} \neq \psi^{\mathrm{X2}}$ require further investigations. Measurements at different velocities v showed that there is indeed a phase shift (and not a time shift) between the signals. Such phase shift is more likely to be optical than electronic in origin, which has been confirmed experimentally by observing that the phase shift is due to an imperfectly perpendicular incidence of the laser beam on the Wollaston prim. The residual oscillations obtained with the simple sum (red curve in Figure 2(b)) are problematic to determine the static and harmonic displacements, as we will show in the following that they lead to periodic non-linearities when normalizing the photocurrents by this sum to compute the contrasts. We can calculate a "corrected sum", defined as:

$$\mathrm{sum}\left[I^{\mathrm{X1,X2}}_{\mathrm{stat}}\right](t) \equiv I^{\mathrm{X1}}_{\mathrm{stat}}(t) + \frac{a^{\mathrm{X1}} b^{\mathrm{X1}}}{a^{\mathrm{X2}} b^{\mathrm{X2}}} I^{\mathrm{X2}}_{\mathrm{stat}}\left(t + \frac{\psi^{\mathrm{X1}} - \psi^{\mathrm{X2}}}{2\pi f_{\mathrm{calib}}}\right). \tag{30}$$

This quantity is represented in blue in Figure 2(b). As expected by construction, this corrected sum exhibits no residual oscillation. However, such a trick of applying a time shift to correct for a phase shift can only be used during the "calibration actuation" at constant velocity v, where the frequency f_{calib} of the interference signals is constant and known. We will propose in the next subsections a method to correct for this phase shift in the general case of an arbitrary and variable velocity v.

Another imperfection can be spotted when comparing the static and harmonic signals coming from the same photodiode. In Figure 2(c) are represented the temporal evolutions of $I^{\mathrm{X1}}_{\mathrm{stat}}$ (in red) and $I^{\mathrm{X1}}_{\mathrm{re}}$ (in blue), together with sinusoidal fits of common frequency f_{calib} (in green). A careful inspection reveal that the sinusoids are not perfectly in quadrature, but there is an additional time shift $\delta t^{\mathrm{X1}}_{\mathrm{stat,dyn}} \sim 0.35$ s. Measurements at different velocities v showed in this case that this is indeed a time shift (and not a phase shift). It is more likely to be electronic than optical in origin, as the two signals are given by the precision multimeter and the lock-in amplifier plugged in series on the same photodiode. We attribute this to a delay in signal acquisition, which exists despite TTL triggering, perhaps due to the different designs of these instruments. This time shift is not due to fitting errors or random noise, as shown by numerically computing a "simple quadrature-shifted sum" as:

$$\mathrm{sum}\left[I^{\mathrm{X1}}_{\mathrm{stat,re}}\right](t) \equiv I^{\mathrm{X1}}_{\mathrm{stat}}(t) + r^{\mathrm{X1}}_{\mathrm{stat,re}} I^{\mathrm{X1}}_{\mathrm{re}}\left(t + \frac{\pi/2}{2\pi f_{\mathrm{calib}}}\right), \tag{31}$$

where $r^{\mathrm{X1}}_{\mathrm{stat,re}}$ compensates for the difference in amplitude between static and harmonic signals, which would be present even in the ideal case (equal to $\phi_{\mathrm{dyn}} \cos\varphi/\sqrt{2}$). This ratio is determined from the sinusoidal fits; it will not be used as a calibration parameter in the next subsection, but only to calculate the simple quadrature-shifted sum. This quantity is represented in red in Figure 2(d), and exhibits residual oscillations at frequency f_{calib}, while sinusoidal signals in perfect quadrature would lead to a constant signal. Note that the harmonic photocurrent has been multiplied by the amplitude ratio (very different from 1, even for ideal signals) and quadrature-shifted by applying a time shift (only possible during the "calibration actuation" at constant velocity v). Such time shift is problematic, as we will show in the following that it leads to periodic non-linearities when combining the static and harmonic signals to

compute the harmonic displacement $H_{\rm dyn}$. We can calculate a "corrected quadrature-shifted sum", where an additional time shift $\delta t^{\rm X1}_{\rm stat,dyn}$ has been applied to the harmonic photocurrent:

$$\begin{aligned}\mathrm{sum}\left[I^{\rm X1}_{\rm stat,re}\right](t) \equiv & I^{\rm X1}_{\rm stat}(t) \\ & + r^{\rm X1}_{\rm stat,re} I^{\rm X1}_{\rm re}\left(t + \frac{\pi/2}{2\pi f_{\rm calib}} + \delta t^{\rm X1}_{\rm stat,dyn}\right).\end{aligned} \tag{32}$$

This quantity is represented in blue in Figure 2(d). As expected by construction, this corrected quadrature-shifted sum exhibits no residual oscillation. As this imperfection is intrinsically a time shift and not a phase shift, it will be easily corrected by numerically time-shifting the harmonic signals (moduli and arguments) to resynchronize them with the static signals.

Calibrations. In order to correct the imperfections presented just before, it is necessary to calibrate them for all the channels. This is done by performing the "calibration actuation" described previously. We recall here its principle: applying to the actuator a quasi-static displacement at constant velocity $v = 2.45$ nm/s (slow enough to fulfil the quasi-static and sampling conditions, fast enough to have little influence of drifts) over a range of ~ 1 μm (to cover ~ 2 periods of static phase) and a harmonic voltage of frequency $\omega/(2\pi) = 30$ Hz (large enough to fulfil the filtering condition, small enough to have the maximum response of the flexure hinge) and of amplitude $V_{\rm dyn} = 0.01$ $\mathrm{V_{rms}}$, corresponding to oscillations of amplitude ~ 1.8 nm (small enough to fulfil the linearity condition, large enough to have little influence of noise). Crucial points are: (i) quasi-static motion is at a constant velocity, so that the signal imperfections pointed out in the previous subsection can be extracted from temporal fittings and phase shifts can be corrected by time shifting the signals; (ii) the amplitude of the harmonic oscillation is small enough that the non-linearities presented in section 5 are negligibly small.

The first calibration consists in fitting the two static signals associated to X arm with sinusoidal fits of common frequency $f_{\rm calib}$ (as in Figure 2(a)) to extract the amplitude ratio $r^{\rm X} = \frac{a^{\rm X1} b^{\rm X1}}{a^{\rm X2} b^{\rm X2}}$ and the phase shift $\Delta^{\rm X} = \psi^{\rm X1} - \psi^{\rm X2}$.

The second calibration consists in fitting the two static and real component of the harmonic signals associated to photodiode 1 in X arm with sinusoidal fits of common frequency $f_{\rm calib}$ (as in Figure 2(c)) to extract the time shift $\delta t^{\rm X1}_{\rm stat,dyn}$.

We can then numerically calculate "corrected contrasts" associated to the X arm, defined as follows only during calibrations:

$$C^{\rm X}_{\rm stat}(t) \equiv \frac{I^{\rm X1}_{\rm stat}(t) - r^{\rm X} I^{\rm X2}_{\rm stat}\left(t + \frac{\Delta^{\rm X}}{2\pi f_{\rm calib}}\right)}{I^{\rm X1}_{\rm stat}(t) + r^{\rm X} I^{\rm X2}_{\rm stat}\left(t + \frac{\Delta^{\rm X}}{2\pi f_{\rm calib}}\right)} \tag{33}$$

$$C^{\rm X}_{\rm mod}(t) \equiv 2\sqrt{2}\frac{I^{\rm X1}_{\rm mod}\left(t + \delta t^{\rm X1}_{\rm stat,dyn}\right)}{I^{\rm X1}_{\rm stat}(t) + r^{\rm X} I^{\rm X2}_{\rm stat}\left(t + \frac{\Delta^{\rm X}}{2\pi f_{\rm calib}}\right)} \tag{34}$$

$$C^{\rm X}_{\rm arg}(t) \equiv I^{\rm X1}_{\rm arg}\left(t + \delta t^{\rm X1}_{\rm stat,dyn}\right). \tag{35}$$

Note that, for analysing the calibration only, the phase shift $\Delta^{\rm X}$ between the pair of static signals is corrected by applying a time shift $+\frac{\Delta^{\rm X}}{2\pi f_{\rm calib}}$ to the signal $I^{\rm X2}_{\rm stat}$, which is possible because the calibration is performed at constant quasi-static velocity (equivalent to constant frequency $f_{\rm calib}$). Together with the correction of the amplitude ratio $r^{\rm X}$ and of the time shift $\delta t^{\rm X1}_{\rm stat,dyn}$ between the static and harmonic signals, this allows to suppress the first type of non-linearities, due to optical and electronic imperfections that are reported in this paper for the first time and which have been described in the previous subsection. The second type of non-linearities, due to large amplitudes of harmonic oscillation and described in section 5 are not present because the oscillation amplitude is kept small for the calibration. One can show that:

$$C^{\rm X}_{\rm stat}(t) \simeq C^{\rm X}_{\rm off} + C^{\rm X}_{\rm amp}\cos\phi_{\rm stat} \tag{36}$$

$$C^{\rm X}_{\rm mod}(t) \simeq C^{\rm X}_{\rm amp}\left|\sin\phi_{\rm stat}\right|\phi_{\rm dyn} \tag{37}$$

$$C^{\rm X}_{\rm arg}(t) \simeq \varphi \text{ if } \sin\phi_{\rm stat} < 0,\ \varphi + \pi \text{ otherwise,} \tag{38}$$

with $C^{\rm X}_{\rm off} = \frac{b^{\rm X2} - b^{\rm X1}}{b^{\rm X2} + b^{\rm X1}}$, $C^{\rm X}_{\rm amp} = \frac{2 b^{\rm X2} b^{\rm X1}}{b^{\rm X2} + b^{\rm X1}}$, and considering that $\psi^{\rm X1} = 0$ without loss of generality as $H_{\rm stat}$ is known to within one constant.

We proceed in the same way for the Y arm, to calculate the corrected contrasts and obtain:

$$C^{\rm Y}_{\rm stat}(t) \simeq C^{\rm Y}_{\rm off} + C^{\rm Y}_{\rm amp}\sin\left(\phi_{\rm stat} + \psi\right) \tag{39}$$

$$C^{\rm Y}_{\rm mod}(t) \simeq C^{\rm Y}_{\rm amp}\left|\cos\left(\phi_{\rm stat} + \psi\right)\right|\phi_{\rm dyn} \tag{40}$$

$$C^{\rm Y}_{\rm arg}(t) \simeq \varphi \text{ if } \cos\left(\phi_{\rm stat} + \psi\right) > 0,\ \varphi + \pi \text{ otherwise,} \tag{41}$$

where $\psi \equiv \psi^{\rm Y1}$.

The third calibration corresponds to the Heydemann corrections applied to the static contrasts. This will allow to correct the well-known imperfections due to optical and electronic imperfections that have been reported in the literature many times. It consists in fitting $C^{\rm Y}_{\rm stat}$ versus $C^{\rm X}_{\rm stat}$ with an elliptical function to obtain the values of $C^{\rm X}_{\rm off}$, $C^{\rm Y}_{\rm off}$, $C^{\rm X}_{\rm amp}$, $C^{\rm Y}_{\rm amp}$ and ψ. In Figure 3(a) is represented $C^{\rm Y}_{\rm stat}$ versus $C^{\rm X}_{\rm stat}$ (the so-called "Lissajous plot"), for "simple contrasts" calculated as for ideal signals (in red, using equations 19 and

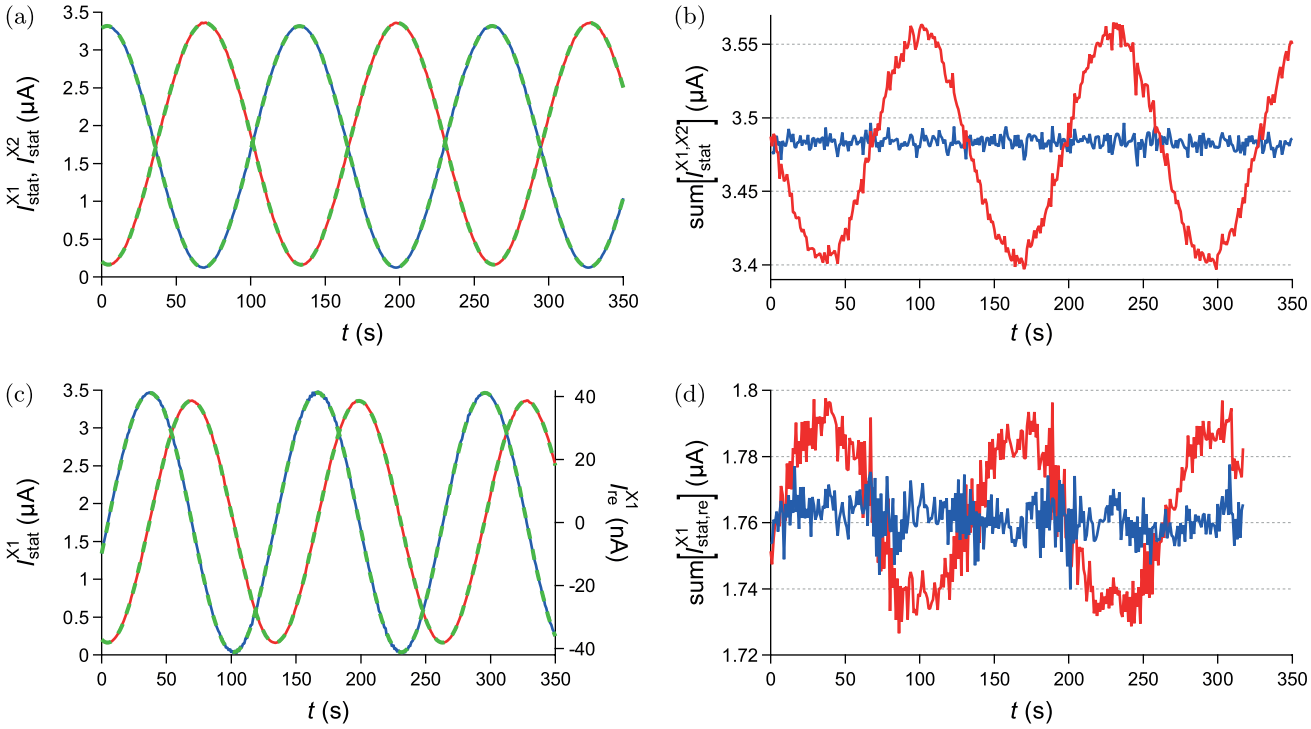

Figure 2. Temporal evolutions of the static and harmonic components of the photocurrents, associated to the X arm, during the "calibration actuation" (i.e. applying a static displacement at constant velocity $v = 2.45$ nm/s and a harmonic voltage of amplitude $V_{\mathrm{dyn}} = 0.01$ $\mathrm{V_{rms}}$ and frequency $\omega/(2\pi) = 30$ Hz to the actuator). (**a**) Static currents measured with photodiodes 1 (in red) and 2 (in blue). The green dashed lines are sinusoidal fits. (**b**) Simple sum (in red) and corrected sum (in blue) of the static currents measured with photodiodes 1 and 2. (**c**) Static current (in red, left axis) and real part of the harmonic current (in blue, right axis) measured with photodiode 1. The green dashed lines are sinusoidal fits. (**d**) Simple quadrature-shifted sum (in red) and corrected quadrature-shifted sum (in blue) of the static current and real part of the harmonic current measured with photodiode 1.

20), "corrected contrast" (in blue, using equations 36 and 39), together with elliptical fits (in green). The two ellipses are slightly different, and a careful inspection suggests that the corrected contrasts are better fitted by the elliptical function. This is better seen in Figure 3(b), where the residuals of the elliptical fits ($\mathrm{res}\left[\mathrm{C}^{\mathrm{X}}_{\mathrm{stat}}\right]$, $\mathrm{res}\left[\mathrm{C}^{\mathrm{Y}}_{\mathrm{stat}}\right]$) are shown as a Lissajous plot. The curve corresponding to simple contrasts (in red) exhibits a so-called trifolium shape [15] of maximum amplitude $\sim 6 \cdot 10^{-3}$, whereas the curve corresponding to corrected contrasts (in blue) exhibits only noise of maximum amplitude $\sim 1 \cdot 10^{-3}$, slightly larger along the ellipse's minor axis than along the ellipse's major axis. The trifolium clearly disappears when correcting for amplitude ratio and phase shift between each pair of photocurrents, which is of utmost importance as we will show in the following that this trifolium leads to periodic non-linearities in the determination of the static and harmonic displacements.

The eleven parameters obtained from the calibrations shown here are summarized in Table 1 (only the ellipse parameters corresponding to the corrected contrasts are given).

Corrections. In this subsection, we will explain how the imperfections presented and calibrated above can be corrected for the analysis of data obtained with an arbitrary and variable velocity v (and not only during the "calibration actuation"). In this case, the phase shift present between the static photocurrents of each pair of photodiodes cannot be corrected by applying a time shift. We define the static contrasts as follows:

$$C^{\mathrm{X}}_{\mathrm{stat}}(t) \equiv \frac{I^{\mathrm{X1}}_{\mathrm{stat}}(t) - r^{\mathrm{X}} I^{\mathrm{X2}}_{\mathrm{stat}}(t)}{I^{\mathrm{X1}}_{\mathrm{stat}}(t) + r^{\mathrm{X}} I^{\mathrm{X2}}_{\mathrm{stat}}(t)} \tag{42}$$

$$C^{\mathrm{Y}}_{\mathrm{stat}}(t) \equiv \frac{I^{\mathrm{Y1}}_{\mathrm{stat}}(t) - r^{\mathrm{Y}} I^{\mathrm{Y2}}_{\mathrm{stat}}(t)}{I^{\mathrm{Y1}}_{\mathrm{stat}}(t) + r^{\mathrm{Y}} I^{\mathrm{Y2}}_{\mathrm{stat}}(t)}. \tag{43}$$

In other words, at this stage we correct for the amplitude ratios r^{X}, r^{Y} but not for the phase shifts Δ^{X} Δ^{Y} between each pair of static signals. The remaining non-linearity comes from the act that the sinusoidal terms do not add up in the numerator and do not cancel out the denominators of equations 42 and 43, because of the phase shifts. In Figure 4(a) are shown typical temporal evolutions of these static contrasts, here during the "calibration actuation". To take these phase shifts into account, we will take advantage that $\left|\Delta^{\mathrm{X}}\right|, \left|\Delta^{\mathrm{Y}}\right| \ll 1$ and expand the static contrasts at first order in Δ^{X} and Δ^{Y}:

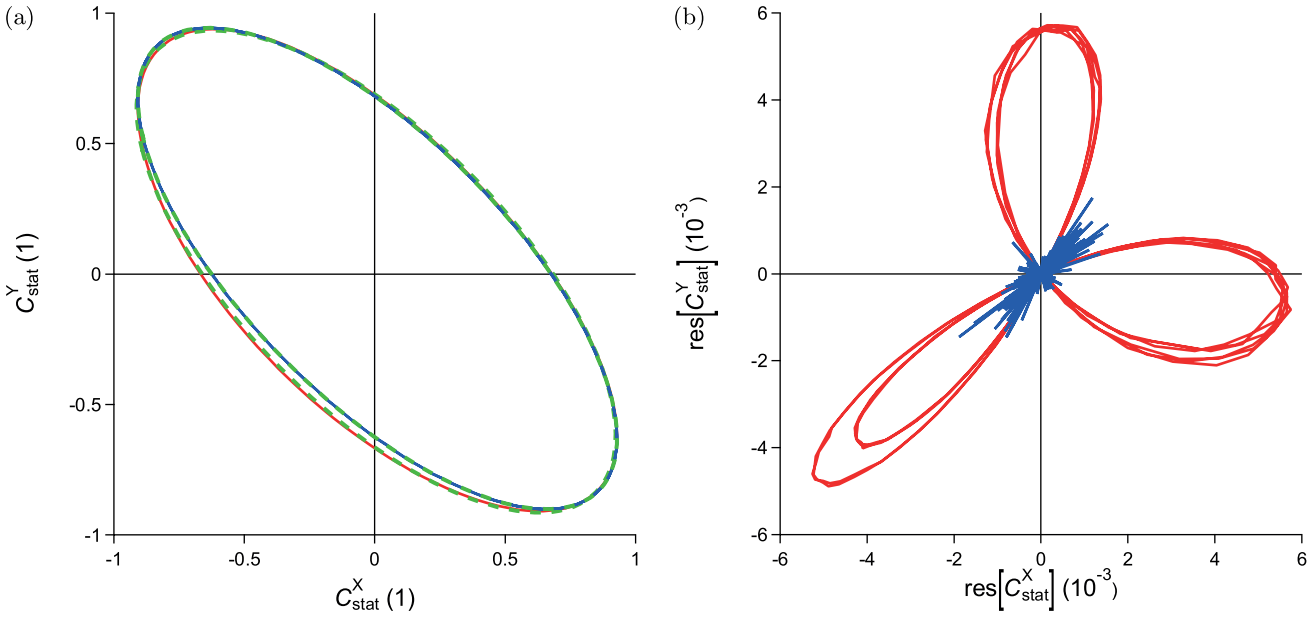

Figure 3. (**a**) Lissajous plot of the static contrasts, associated to the X and Y arms, during the "calibration actuation". The red curve is obtained with static contrasts calculated without correcting (in red) and while correcting (in blue) for amplitude ratio and phase shift between each pair of photocurrents. The green dashed lines are elliptical fits. (**b**) Lissajous plot of the residuals of the elliptical fits of the static contrasts, calculated without correcting (in red) and while correcting (in blue) for amplitude ratio and phase shift between each pair of photocurrents.

Table 1. Calibration parameters obtained for the data shown in this paper.

r^{X} (1)	Δ^{X} (rad)	$\delta t^{\mathrm{X1}}_{\mathrm{stat,dyn}}$ (s)	r^{Y} (1)	Δ^{Y} (rad)	$\delta t^{\mathrm{Y1}}_{\mathrm{stat,dyn}}$ (s)	$C^{\mathrm{X}}_{\mathrm{off}}$ (1)	$C^{\mathrm{Y}}_{\mathrm{off}}$ (1)	$C^{\mathrm{X}}_{\mathrm{amp}}$ (1)	$C^{\mathrm{Y}}_{\mathrm{amp}}$ (1)	ψ (rad)
0.999	-0.0483	-0.347	1.091	0.0218	-0.345	0.0102	0.0211	0.918	0.922	-0.783

$$C^{\mathrm{X}}_{\mathrm{stat}} \simeq \left[C^{\mathrm{X}}_{\mathrm{off}} - \left(1+C^{\mathrm{X}}_{\mathrm{off}}\right)\frac{1}{2}C^{\mathrm{X}}_{\mathrm{amp}}\Delta^{\mathrm{X}}\sin\phi_{\mathrm{stat}}\right] + C^{\mathrm{X}}_{\mathrm{amp}}\cos\phi_{\mathrm{stat}}\left[1-\frac{1}{2}C^{\mathrm{X}}_{\mathrm{amp}}\Delta^{\mathrm{X}}\sin\phi_{\mathrm{stat}}\right] \quad (44)$$

$$C^{\mathrm{Y}}_{\mathrm{stat}} \simeq \left[C^{\mathrm{Y}}_{\mathrm{off}} + \left(1+C^{\mathrm{Y}}_{\mathrm{off}}\right)\frac{1}{2}C^{\mathrm{Y}}_{\mathrm{amp}}\Delta^{\mathrm{Y}}\cos\left(\phi_{\mathrm{stat}}+\psi\right)\right] + C^{\mathrm{Y}}_{\mathrm{amp}}\sin\left(\phi_{\mathrm{stat}}+\psi\right)\left[1+\frac{1}{2}C^{\mathrm{Y}}_{\mathrm{amp}}\Delta^{\mathrm{Y}}\cos\left(\phi_{\mathrm{stat}}+\psi\right)\right]. \quad (45)$$

At zero order we recover the ellipse equations (equations 36 and 39). At first order, we observe that the phase shifts tend to slightly modify the center and amplitudes of the ellipse. This is only approximate, as the correction terms depend themselves on the variable ϕ_{stat} of this parametric equation.

Conversely, we can express the cosine and sine of the static phase ϕ_{stat} as:

$$\cos\phi_{\mathrm{stat}} \simeq \frac{C^{\mathrm{X}}_{\mathrm{stat}} - C^{\mathrm{X}}_{\mathrm{off}} + \left(1+C^{\mathrm{X}}_{\mathrm{off}}\right)\frac{1}{2}C^{\mathrm{X}}_{\mathrm{amp}}\Delta^{\mathrm{X}}\sin\phi_{\mathrm{stat}}}{C^{\mathrm{X}}_{\mathrm{amp}}\left[1-\frac{1}{2}C^{\mathrm{X}}_{\mathrm{amp}}\Delta^{\mathrm{X}}\sin\phi_{\mathrm{stat}}\right]} \quad (46)$$

$$\sin\phi_{\mathrm{stat}} \simeq \left[\frac{C^{\mathrm{Y}}_{\mathrm{stat}} - C^{\mathrm{Y}}_{\mathrm{off}} - \left(1+C^{\mathrm{Y}}_{\mathrm{off}}\right)\frac{1}{2}C^{\mathrm{Y}}_{\mathrm{amp}}\Delta^{\mathrm{Y}}\cos\left(\phi_{\mathrm{stat}}+\psi\right)}{C^{\mathrm{Y}}_{\mathrm{amp}}\left[1+\frac{1}{2}C^{\mathrm{Y}}_{\mathrm{amp}}\Delta^{\mathrm{Y}}\cos\left(\phi_{\mathrm{stat}}+\psi\right)\right]} - \cos\phi_{\mathrm{stat}}\sin\psi\right]\frac{1}{\cos\psi}. \quad (47)$$

The static phase ϕ_{stat} can be deduced for each pair $(C^{\mathrm{X}}_{\mathrm{stat}}, C^{\mathrm{Y}}_{\mathrm{stat}})$ measured experimentally, given that all parameters have been calibrated. A subtlety is that the static phase ϕ_{stat} to be determined also appears in the right-hand sides. Thus, correcting the non-linearities due to the phase shifts requires to solve these self-consistent equations. As these corrections are small, we can proceed iteratively:

- we first perform the calculation as if there were no phase shifts (i.e., we assume $\Delta^{\mathrm{X}} = \Delta^{\mathrm{Y}} = 0$) to get a zeroth-order estimate $\phi_{\mathrm{stat},0}$,
- we secondly restore their calibrated values to Δ^{X} and Δ^{Y}, use $\phi_{\mathrm{stat},0}$ in the right-hand sides

of equations 46 and 47 to obtain a first-order estimate $\phi_{\mathrm{stat},1}$,

- we then iterate the previous step as many times as necessary.

In practice, we found that $N \sim 3$ iterations are enough for the value of $\phi_{\mathrm{stat,N}}$ to converge within 1%. The static displacement H_{stat} can then be deduced.

For the dynamic analysis to be at the same time insensitive to any intensity fluctuations of the laser, and not impacted by the phase shift between each pair of photodiodes, we define corrected sums for the static photocurrents as follows:

$$\begin{aligned}\mathrm{sum}\left[\mathrm{I}_{\mathrm{stat}}^{\mathrm{X1,X2}}\right](\mathrm{t}) \equiv &\left[I_{\mathrm{stat}}^{\mathrm{X1}}(t) + r^{\mathrm{X}} I_{\mathrm{stat}}^{\mathrm{X2}}(t)\right] \\ &\times \left[1 + \frac{1}{2} C_{\mathrm{amp}}^{\mathrm{X}} \Delta^{\mathrm{X}} \sin\phi_{\mathrm{stat}}\right]\end{aligned} \tag{48}$$

$$\begin{aligned}\mathrm{sum}\left[\mathrm{I}_{\mathrm{stat}}^{\mathrm{Y1,Y2}}\right](\mathrm{t}) \equiv &\left[I_{\mathrm{stat}}^{\mathrm{Y1}}(t) + r^{\mathrm{Y}} I_{\mathrm{stat}}^{\mathrm{Y2}}(t)\right] \\ &\times \left[1 - \frac{1}{2} C_{\mathrm{amp}}^{\mathrm{Y}} \Delta^{\mathrm{Y}} \cos\left(\phi_{\mathrm{stat}} + \psi\right)\right].\end{aligned} \tag{49}$$

We use these corrected sums to normalize the harmonic photocurrents and define the dynamic contrasts as, in the case of the X arm:

$$C_{\mathrm{mod}}^{\mathrm{X}}(t) \equiv 2\sqrt{2} \frac{I_{\mathrm{mod}}^{\mathrm{X1}}\left(t + \delta t_{\mathrm{stat,dyn}}^{\mathrm{X1}}\right)}{\mathrm{sum}\left[\mathrm{I}_{\mathrm{stat}}^{\mathrm{X1,X2}}\right](\mathrm{t})} \tag{50}$$

$$C_{\mathrm{arg}}^{\mathrm{X}}(t) \equiv I_{\mathrm{arg}}^{\mathrm{X1}}\left(t + \delta t_{\mathrm{stat,dyn}}^{\mathrm{X1}}\right). \tag{51}$$

We proceed similarly for the Y arm. Therefore, these dynamic contrasts contain corrections for the amplitude ratios r^{X}, r^{Y} and the phase shifts Δ^{X} Δ^{Y} between each pair of static signals, and for the time shifts $\delta t_{\mathrm{stat,dyn}}^{\mathrm{X1}}$, $\delta t_{\mathrm{stat,dyn}}^{\mathrm{Y1}}$ between the static and harmonic signals coming from the same photodiode. Note that in general the time shifts are a fraction of the sampling period $T = 1$ s, therefore linear interpolations are performed in order to evaluate the harmonic photocurrents at shifted times. In Figure 4(b) and (c) are respectively shown typical temporal evolutions of the modulus and arguments of these dynamic contrasts, here during the "calibration actuation". With such definitions, one can show that we recover the expressions for the dynamic contrasts given by the equations 37, 38, 40 and 41.

The harmonic displacement H_{dyn} is simply obtained by numerically combining the dynamic contrasts with the static phase:

$$\begin{aligned}x \equiv &- C_{\mathrm{mod}}^{\mathrm{X}} \cos\left(C_{\mathrm{arg}}^{\mathrm{X}}\right) C_{\mathrm{amp}}^{\mathrm{Y}} \sin\left(\phi_{\mathrm{stat}} + \psi\right) \\ &+ C_{\mathrm{mod}}^{\mathrm{Y}} \cos\left(C_{\mathrm{arg}}^{\mathrm{Y}}\right) C_{\mathrm{amp}}^{\mathrm{X}} \cos\phi_{\mathrm{stat}}\end{aligned} \tag{52}$$

$$\begin{aligned}y \equiv &- C_{\mathrm{mod}}^{\mathrm{X}} \sin\left(C_{\mathrm{arg}}^{\mathrm{X}}\right) C_{\mathrm{amp}}^{\mathrm{Y}} \sin\left(\phi_{\mathrm{stat}} + \psi\right) \\ &+ C_{\mathrm{mod}}^{\mathrm{Y}} \sin\left(C_{\mathrm{arg}}^{\mathrm{Y}}\right) C_{\mathrm{amp}}^{\mathrm{X}} \cos\phi_{\mathrm{stat}}\end{aligned} \tag{53}$$

$$H_{\mathrm{dyn}} = \frac{\lambda}{4\pi} \frac{\sqrt{x^2 + y^2}}{C_{\mathrm{amp}}^{\mathrm{X}} C_{\mathrm{amp}}^{\mathrm{Y}} \cos\psi}. \tag{54}$$

Results. Figure 5(a) shows the temporal evolution of the static displacement H_{stat} during the "calibration actuation", computed numerically from the experimentally measured photocurrents thanks to the calibrated parameters, without correcting (in red) and while correcting (in blue) for amplitude ratios, phase shifts and time shifts. The red curve therefore corresponds to the application of the Heydemann corrections only. At first glance, the two analyses produce two very similar signals which vary linearly with time, and linear fits (in green) provide the same slope, equal to $v = 2.45$ nm/s. However the residuals on the fits (shown on top) are significantly different. The signal obtained with Heydemann corrections only (in red) exhibits periodic variations, with a peak-peak amplitude of ~ 3.8 nm and a period corresponding to the interferogram's one (i.e., $\frac{\lambda}{2v}$). On the contrary, the signal obtained with all the corrections (in blue) does not present such periodic variations, but only random noise of standard deviation ~ 0.11 nm.

Figure 5(b) shows the temporal evolution of the harmonic displacement H_{dyn} deduced simultaneously, without correcting (in red) and while correcting (in blue) for amplitude ratios, phase shifts and time shifts. The signal obtained with Heydemann corrections only (in red) exhibits periodic variations at the interferogram's period, with a peak-peak amplitude of ~ 0.25 nm, corresponding to $\sim 14\%$ of the nominal harmonic displacement. On the contrary, the signal obtained with all the corrections (in blue) does not present such periodic variations, but only random noise of standard deviation ~ 8.8 pm around a mean value of ~ 1.831 nm, hence a relative standard deviation of $\sim 0.5\%$.

This clearly shows that optical and electronic imperfections lead to periodic non-linearities in the measurement of the static and harmonic displacements. More precisely, these imperfections are amplitude ratios and phase shifts between each pair of static signals, and the time shifts between the static and harmonic signals coming from the same photodiode. The procedure proposed to correct these imperfections produces satisfying results, removing all periodic non-linearities, or at least reducing them below the noise level. It is important to note that it is

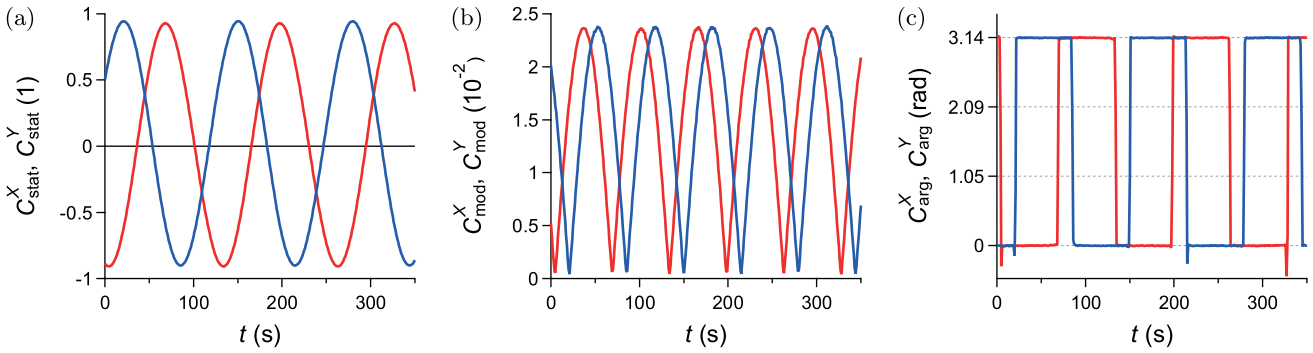

Figure 4. Temporal evolutions of the static and dynamic contrasts, associated to the X arm (in red) and the Y arm (in blue), during the "calibration actuation": (**a**) static contrasts, (**b**) modulus of the dynamic contrast, (**c**) argument of the dynamic contrast. Here the static contrasts are calculated while correcting for amplitude ratio but not for phase shift between each pair of static photocurrents, whereas dynamic contrasts are calculated while correcting for these two imperfections and for time shifts between harmonic and static currents measured for each photodiode.

not just one or two of these imperfections that need to be corrected, but all three, in order to remove all periodic non-linearities. Providing that the sampling condition (equation 7) is satisfied (see section 6), these corrections have no influence on the random noise that can be observed on the deduced displacements. This noise was already present on the raw photocurrents, and probably has several sources: vibrations of the mechanical assembly, fluctuations of the laser frequency, shot noise of the photodiodes, parasitic signals in the electronics [16], etc. The characterization and reduction of this noise is beyond the scope of this article, which focuses on the correction of non-linearities in quadrature phase differential interferometry.

5. Correction of non-linearities due to large amplitudes of harmonic oscillation

Generalisation. The analysis presented so far is only valid when the linearity condition is verified, i.e., $\phi_{\rm dyn} \ll 1$ (equation 5). If the harmonic displacement $H_{\rm dyn}$ is not small enough, the linearisation given as equation 9 is no longer valid. Nevertheless, it is possible to expand the phase-modulated photocurrent in Fourier series, the coefficients of the series being expressed by the Bessel functions of first kind [13, 17, 18]. In the following, we write equations only for channel X1 as similar ones can be obtained for all channels, and for the sake of simplicity we will first consider that the imperfections presented in the previous section 4 are not present. It can be mathematically shown that:

$$I^{\rm X1} \simeq \frac{I_0}{2}\Bigg[1+\Bigg\{J_0(\phi_{\rm dyn}) +2\sum_{p=1}^{+\infty}(-1)^p J_{2p}(\phi_{\rm dyn})\cos((2p)\omega t)\Bigg\}\cos\phi_{\rm stat} -\Bigg\{2\sum_{p=0}^{+\infty}(-1)^p J_{2p+1}(\phi_{\rm dyn})\cos((2p+1)\omega t)\Bigg\}\sin\phi_{\rm stat}\Bigg], \tag{55}$$

where J_k are the Bessel functions of first kind of order k.

We identify the static component, measured by the precision multimeters, as:

$$I^{\rm X1}_{\rm stat} \simeq \frac{I_0}{2}\left[1+J_0(\phi_{\rm dyn})\cos\phi_{\rm stat}\right], \tag{56}$$

$$J_0(\phi_{\rm dyn}) = \sum_{n=0}^{+\infty}\frac{(-1)^n}{(n!)^2}\left(\frac{\phi_{\rm dyn}}{2}\right)^{2n} \tag{57}$$

$$= 1-\frac{{\phi_{\rm dyn}}^2}{4}+\frac{{\phi_{\rm dyn}}^4}{64}-\frac{{\phi_{\rm dyn}}^6}{2304}+\ldots \tag{58}$$

The RMS modulus of the harmonic component at the working frequency $\omega/(2\pi)$, measured by the lock-in amplifiers, is equal to:

$$I^{\rm X1}_{\rm mod} \simeq \frac{I_0}{2\sqrt{2}}\left|\sin\phi_{\rm stat}\right|\phi_{\rm dyn}\frac{2J_1(\phi_{\rm dyn})}{\phi_{\rm dyn}}, \tag{59}$$

$$\frac{2J_1(\phi_{\rm dyn})}{\phi_{\rm dyn}} = \sum_{n=0}^{+\infty}\frac{(-1)^n}{n!(n+1)!}\left(\frac{\phi_{\rm dyn}}{2}\right)^{2n} \tag{60}$$

$$= 1-\frac{{\phi_{\rm dyn}}^2}{8}+\frac{{\phi_{\rm dyn}}^4}{192}-\frac{{\phi_{\rm dyn}}^6}{9216}+\ldots \tag{61}$$

We note that the argument of the harmonic component at this frequency is still given by equation 18.

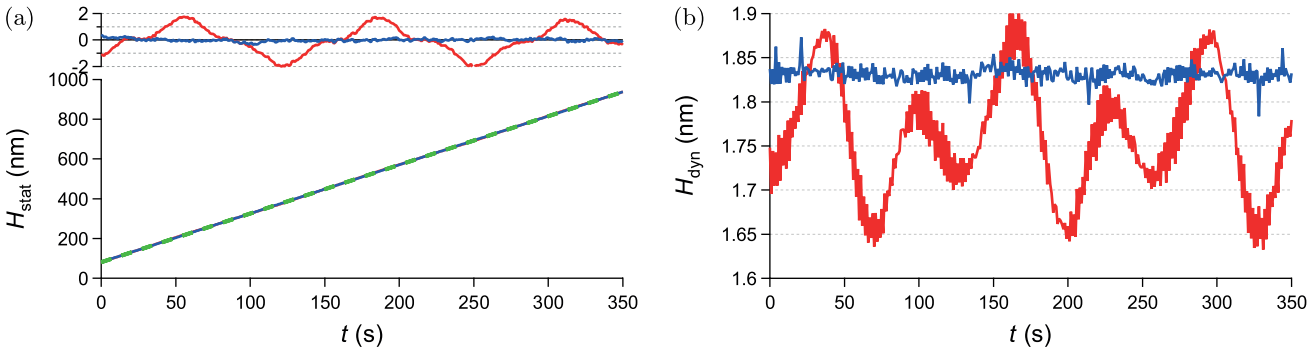

Figure 5. Temporal evolutions of the static and harmonic displacements obtained during the "calibration actuation", with Heydemann corrections only (in red) and with all the corrections (in blue). (**a**) Bottom: static displacements, and linear fits (green dashed lines). Top: corresponding residuals of the fits. (**b**) Modulus of the harmonic displacement.

This second type of non-linearity is explicitly revealed by the presence of the harmonic phase $\phi_{\rm dyn}$ in Bessel functions. Comparing the equations 56 and 59 to the equations 12 and 17 obtained with the linear analysis, we observe that a large harmonic displacement $H_{\rm dyn}$ has two effects:

- reducing the envelope of the static interferogram by a factor $J_0(\phi_{\rm dyn})$,
- reducing the modulus of the harmonic signal by a factor $\frac{2J_1(\phi_{\rm dyn})}{\phi_{\rm dyn}}$.

The same non-linear analysis can be performed for all channels, and also in the case where the imperfections presented in the previous section 4 are present. Finally, a large harmonic displacement $H_{\rm dyn}$ has two effects on the different contrasts:

- reducing the amplitude of the ellipse formed by the static contrasts by a factor $J_0(\phi_{\rm dyn})$ (same reduction along the two axis X and Y, the center being invariant),
- reducing the modulus of the dynamic contrasts by a factor $\frac{2J_1(\phi_{\rm dyn})}{\phi_{\rm dyn}}$ (same reduction for X and Y).

Corrections. These effects induced by a large amplitude of harmonic oscillation can be taken into account to calculate the static and harmonic displacements.

The equations 46 and 47 giving the static displacement should be adapted, by dividing by $J_0(\phi_{\rm dyn})$ each term where $\phi_{\rm stat}$ appears (three times for each equation). The equations 52 and 53 together with 54 giving the harmonic displacement are modified by dividing by $\frac{2J_1(\phi_{\rm dyn})}{\phi_{\rm dyn}}$ each term where $C^{\rm X}_{\rm mod}$ or $C^{\rm Y}_{\rm mod}$ appears (twice in the first two equations).

The Bessel functions J_0 and J_1 are easily calculated numerically by using the expansions 58 and 61 up to a required order n (note that only even order are non zero). In the following, and unless otherwise indicated, these corrective terms have been calculated to order 10. A difficulty is that $\phi_{\rm dyn}$ should be known to determine $\phi_{\rm stat}$ and $\phi_{\rm dyn}$. As the corrections coming from the non-linear analysis are small, we can proceed iteratively here too:

- we first perform the calculation with the linear analysis (i.e., we do not include any $J_0(\phi_{\rm dyn})$ or $\frac{2J_1(\phi_{\rm dyn})}{\phi_{\rm dyn}}$ factors) to get estimates $\phi_{\rm stat,0}$ and $\phi_{\rm dyn,0}$,
- we secondly perform the non-linear analysis, including $J_0(\phi_{\rm dyn})$ and $\frac{2J_1(\phi_{\rm dyn})}{\phi_{\rm dyn}}$ factors to obtain estimates $\phi_{\rm stat,1}$ and $\phi_{\rm dyn,1}$,
- we then iterate the previous step as many times as necessary.

In practice, we found that $M \sim 2$ iterations are enough for the value of $\phi_{\rm stat,M}$ and $\phi_{\rm dyn,M}$ to converge within 1%. Note that for each of the $M = 2$ steps of this iterative procedure to take account of large amplitudes of harmonic oscillation, another iterative procedure with $N = 3$ steps is performed to take account of phase shifts between the static signals for each pair of photodiodes (as explained in previous section 4). Therefore the calculation involves a total of $M \times N = 6$ steps.

Results. Figure 6(a) shows a Lissajous plot of the static contrasts defined as equations 42 and 43 (in red), when successively applying harmonic voltages of amplitudes $V_{\rm dyn} = 0.008, 0.08$ and 0.2 $V_{\rm rms}$ to the actuator. We clearly see that the interferometer covers different ellipses, of same center but of amplitude decreasing with the amplitude of harmonic oscillation. Corrected contrasts, used only for this graph, can be calculated by dividing the distance to center by the factor $J_0(\phi_{\rm dyn})$. The result is shown in blue, and we see that the data obtained for different amplitudes of harmonic oscillation are now nicely superimposed on the largest ellipse. This graphically allows to check that the influence of a large amplitude of harmonic oscillation on the static contrasts is well described

by our analysis, and that the correction proposed in the previous subsection is appropriate. This is important, because we observed that if the influence of a large amplitude of harmonic oscillation on the static contrasts was not corrected, this would lead to periodic non-linearities in the determination of the static and harmonic displacements (similar to the ones shown in Figure 5).

In Figure 6(b) is represented the harmonic displacement $H_{\rm dyn}$ as a function of the rms amplitude $V_{\rm dyn}$ of the harmonic voltage applied to the actuator, in log-log scales. The red markers (resp. blue markers) are the obtained without correcting (resp. while correcting) for the factor $\frac{2J_1(\phi_{\rm dyn})}{\phi_{\rm dyn}}$ in the modulus of the harmonic signals. The corrected data exhibit a perfect linear behaviour over 2 decades of harmonic displacements, from ~ 0.7 nm to ~ 70 nm. The blue line is a linear fit of the form:

$$H_{\rm dyn} = \alpha(30\text{ Hz}) \times \mathrm{V}_{\rm dyn}, \tag{62}$$

with $\alpha_{30\text{ Hz}} = 181.1 \pm 0.6$ nm/$\mathrm{V}_{\rm rms}$ which is the electro-mechanical response coefficient of our actuator at 30 Hz. This proves that the actuator response is linear and that the influence of a large amplitude of harmonic oscillation on the dynamic contrasts is well corrected by our analysis. On the contrary, the uncorrected data exhibit a sub-linear shape. The red curve is a prediction of the form:

$$H_{\rm dyn} = \frac{\lambda}{4\pi} \times 2J_1\left(\frac{4\pi\alpha(30\text{ Hz})\mathrm{V}_{\rm dyn}}{\lambda}\right). \tag{63}$$

This theoretical curve nicely passes through the experimental points, again showing that the influence of a large amplitude of harmonic oscillation on the dynamic contrasts is well corrected by our analysis. If the influence of a large amplitude of harmonic oscillation on the dynamic contrasts was not corrected, this would lead to an underestimation of the harmonic displacement. We can use this criterion to precisely specify the range of validity of the linear analysis: for $H_{\rm dyn} = 10$ nm the linear analysis underestimate the harmonic displacement by only 0.03%, for $H_{\rm dyn} = 17$ nm the linear analysis underestimate the harmonic displacement by 1% and for $H_{\rm dyn} = 70$ nm the linear analysis underestimate the harmonic displacement by 22%. Thus we can refine the linearity condition given in equation 5 by saying that the linear analysis holds within $\sim 1\%$ for harmonic displacements lower than $\sim$ 20 nm.

An important aspect is to choose the order n up to which the expansions 58 and 61 are used to calculate the Bessel functions J_0 and J_1. Figure 6(c) shows on top the calculated harmonic displacement as a function of the calculation order, for a harmonic voltage of amplitude $V_{\rm dyn} = 0.4$ $\mathrm{V}_{\rm rms}$ applied to the actuator. The black dashed line is the value for $n = 10$ equal to $\sim$ 72 nm, and the markers in blue (resp. in red) indicate values smaller (resp. larger) than the value for $n = 10$. At the beginning the linear analysis underestimates the harmonic displacement, but then the terms of alternating signs coming from the non-linear correction lead to an damped oscillatory shape. The bottom graph shows in semi-log scales the absolute value of the relative error committed when stopping the calculation at a given order n compared to order $n = 10$, defined as:

$$|\mathrm{err}\,[\mathrm{H_{dyn}}]| = \frac{|H_{\rm dyn}(n) - H_{\rm dyn}(n=10)|}{H_{\rm dyn}(n=10)}. \tag{64}$$

The markers in blue (resp. in red) indicate negative (resp. positive) errors. The error continuously decreases with the correction order, and the black dashed line suggests this decrease is exponential with an error that is divided by ~ 50 every time a correction term is added (n incremented by 2, the odd terms being zero). This characterisation allows to choose the order n as a function of the desired precision in the determination of the harmonic displacement. For all the data presented in this paper, we have used $n = 10$ to make this error negligibly small compared with the noise and drift of the experimental data.

6. Robustness of the corrections

So far we have presented data obtained for a single velocity $v = 2.45$ nm/s and a single frequency $\omega/(2\pi) = 30$ Hz, and in cases where the two types of non-linearities presented in the previous sections 4 and 5 were not present at the time. The objective of this section is to assess the robustness of the analysis, when varying the velocity and frequency, and when the two types of non-linearities are present simultaneously.

Velocity. In Figure 7(a) is shown the temporal evolution of the harmonic displacement when applying a harmonic voltage of amplitude $V_{\rm dyn} = 0.02$ $\mathrm{V}_{\rm rms}$ to the actuator, for different quasi-static velocities. The time axis is rescaled by the velocity v in order to be able to compare the signals graphically. For $v = 0.20$ nm/s (smallest velocity, in red) and $v = 2.0$ nm/s (velocity typically used for calibration, in blue), the signals present no periodic non-linearities but random noise of standard deviation of 7 pm around a mean value of 3.653 nm, hence a relative standard deviation of 0.2%. In contrast, the signal for $v = 20$ nm/s (in green) presents a slightly smaller mean value of 3.587 nm and a significantly larger standard deviation of 0.2 nm, corresponding to a

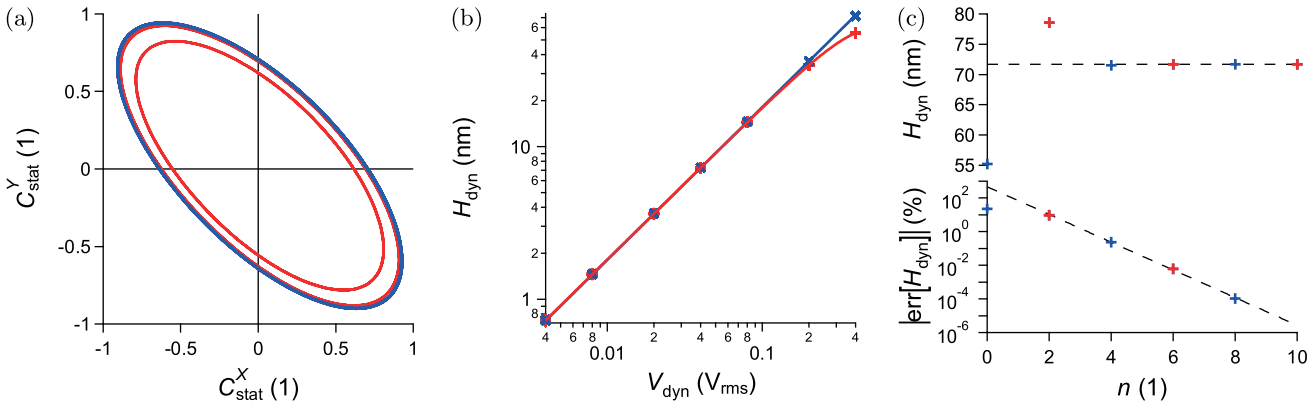

Figure 6. (**a**) Lissajous plot of the static contrasts, when successively applying harmonic voltages of amplitudes $V_{\mathrm{dyn}} = 0.008, 0.08$ and 0.2 $\mathrm{V_{rms}}$ and simultaneously a static displacement at velocity $v = 2.45$ nm/s to the actuator. The red curves are the raw signals, whereas the blue curves are obtained by correcting for non-linear effects. (**b**) Modulus of the harmonic displacement as a function of the rms amplitude of the harmonic voltage applied to the actuator, in log-log scales, while applying no quasi-static motion. The red markers are the raw measurements, whereas the blue markers are obtained by correcting for non-linear effects. The blue curve is a linear fit of the corrected data, whereas the red curve is the prediction from the non-linear analysis given by equation 63. (**c**) Top: Modulus of the harmonic displacement, for a harmonic voltage of amplitude $V_{\mathrm{dyn}} = 0.4$ $\mathrm{V_{rms}}$ applied to the actuator, as a function of the correction order n. The black dashed line is the value for $n = 10$, and the markers in blue (resp. in red) indicate values smaller (resp. larger) than the value for $n = 10$. Bottom: Corresponding absolute value of the relative error on the modulus of the harmonic displacement as a function of the correction order n, in semi-log scales. The black dashed line is an exponential fit, excluding the values for $n = 0$ and $n = 10$.

relative standard deviation of 5%. Of course, for these three runs the true harmonic displacement was exactly the same constant, and the differences observed here are measurement artefacts. We think that this velocity effect is due to the sampling condition (equation 7) that no longer holds.

We have systematically characterised the influence of the velocity on the average and the fluctuations of the harmonic displacement. Figure 7(b) shows how the mean of the harmonic displacement is modified relatively to its value at the smallest velocity of 0.2 nm/s (considered as the true harmonic displacement), in absolute value (quantity labelled as $|\mathrm{err}\left[\langle \mathrm{H_{dyn}} \rangle\right]|$, in red, left axis). The same graph also shows how the standard deviation of the harmonic displacement varies relatively to the true harmonic displacement (quantity labelled as $\mathrm{err}\left[\sigma\left(\mathrm{H_{dyn}}\right)\right]$), in blue, right axis). At small velocities, the determination of the harmonic displacement is the most accurate, precise and independent of the velocity. At large velocities, the determination of the harmonic displacement becomes clearly dependent on the velocity, with the accuracy and more significantly the precision which are all the more degraded than the velocity is large. We can refine the sampling condition given in equation 7 by saying that the analysis holds within $\sim 1\%$ in accuracy and precision for velocities lower than ~ 5 nm/s for a sampling period $T = 1$ s.

Combined corrections. An important question is whether the methods proposed to correct for the two types of non-linearities, due to optical and electronic imperfections (section 4), and due to large amplitudes of harmonic oscillation (section 5), work when these two types of non-linearities are present simultaneously. It can be evaluated by checking whether or not the harmonic displacement exhibits periodic oscillations when applying a static displacement at a finite velocity $v = 2.45$ nm/s and a harmonic voltage of very large amplitude. To be able to graphically compare the result with signals obtained at small harmonic voltages, we define the relative error on the harmonic displacement as:

$$\mathrm{err}\left[\mathrm{H_{dyn}}\right] = \frac{\mathrm{H_{dyn}} - \langle \mathrm{H_{dyn}} \rangle}{\langle \mathrm{H_{dyn}} \rangle}, \tag{65}$$

where $\langle \cdot \rangle$ indicates a time average. Figure 7(c) shows the temporal evolution of this quantity when applying a static displacement at velocity $v = 2.45$ nm/s and a harmonic voltage of amplitude $V_{\mathrm{dyn}} = 0.008$ $\mathrm{V_{rms}}$ (in red), $V_{\mathrm{dyn}} = 0.08$ $\mathrm{V_{rms}}$ (in blue) or $V_{\mathrm{dyn}} = 0.2$ $\mathrm{V_{rms}}$ (in green) to the actuator, corresponding to average harmonic displacements of respectively 1.5 nm, 15 nm and 36 nm. We see that no periodic non-linearities are observed for either curves, and in particular for the one with the largest harmonic voltage. The proposed corrections work very satisfactorily even when both types of non-linearity are present simultaneously.

We can note a slightly larger random noise for the lowest harmonic voltage (respectively 0.43%, 0.29% and 0.30%). This is explained by some instrumental noise which is independent of the amplitude of the harmonic displacement, and which has therefore a relatively stronger impact on the measurements in the case of small harmonic displacements.

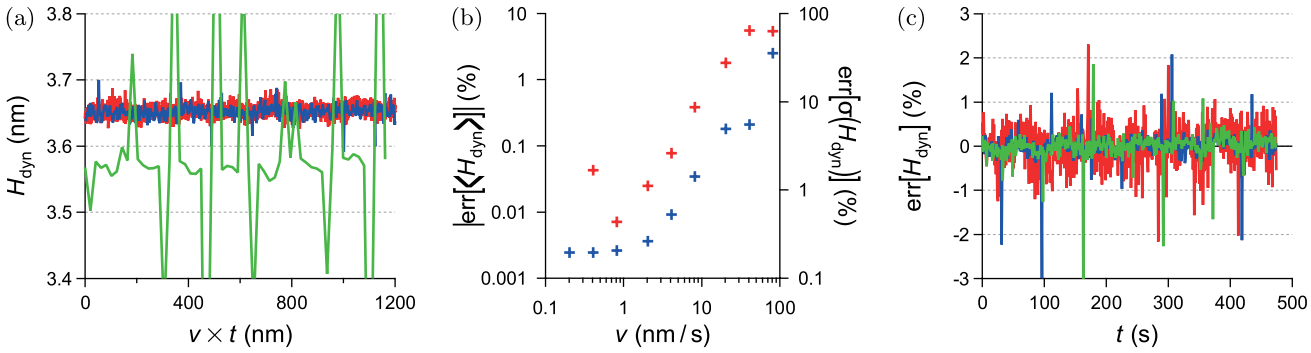

Figure 7. (**a**) Temporal evolution of the modulus of the harmonic displacement, when applying a harmonic voltage of amplitude $V_{dyn} = 0.02$ V_{rms} to the actuator, and a static displacement at velocity $v = 0.20$ nm/s (in red), $v = 2.0$ nm/s (in blue) or $v = 20$ nm/s (in green). Time has been multiplied by the corresponding velocity, so that the signals can be compared. (**b**) Relative error on the average (in red, left axis) and relative error on the standard deviation (in blue, right axis) over the measured modulus of the harmonic displacement, as a function of the static velocity, in semi-log scales. (**c**) Temporal evolution of the relative error on the modulus of the harmonic displacement, when applying a static displacement at velocity $v = 2.45$ nm/s and a harmonic voltage of amplitude $V_{dyn} = 0.008$ V_{rms} (in red), $V_{dyn} = 0.08$ V_{rms} (in blue) or $V_{dyn} = 0.2$ V_{rms} (in green) to the actuator.

Frequency. Figure 8(a) shows the variation of the harmonic displacement when scanning the working frequency $\omega/(2\pi)$ from 10 Hz to 500 Hz, for four different harmonic voltages: $V_{dyn} = 0.0027$ V_{rms} (in blue), $V_{dyn} = 0.013$ V_{rms} (in green), $V_{dyn} = 0.053$ V_{rms} (in yellow) or $V_{dyn} = 0.27$ V_{rms} (in red). Note that the measured harmonic displacements range between ~ 20 pm and ~ 80 nm. The general shape is reminiscent of the electro-mechanical response of our actuator, described in section 2, which can be modelled as a damped mass-spring system with a resonance frequency around 115 Hz. The dips in the curves around 115 Hz, all the more pronounced that the harmonic voltage is large, are due to an electronic saturation of the lock-in amplifier inputs, limiting the measurements to maximum of ~ 80 nm. This saturation could be removed by inserting a current divider, not implemented here. We also remark peaks every multiple of 50 Hz, all the more visible that the harmonic voltage is small. This is 50 Hz electronic noise coming from the power supply and irradiating the cables connecting the photodiodes to the amperemeters, which is present even if these cables are ground shielded. Overall, one can say that the range of measurable harmonic displacements is limited here by the electronics, and not by the signal analysis described in this article.

In Figure 8(b) the harmonic displacements H_{dyn} are rescaled by the harmonic voltages V_{dyn}, and we observe that all the curves collapse on a single master curve (except for points corresponding to saturation of the lock-in amplifier inputs and to 50 Hz noise). This electro-mechanical response can be fitted with a simple harmonic oscillator model (black dashed line), of the form:

$$\alpha(\omega) \equiv \frac{H_{dyn}}{V_{dyn}} = \frac{A}{\sqrt{\left(1 - (\omega/\omega_0)^2\right)^2 + \left((\omega/\omega_0)/Q\right)^2}}, \tag{66}$$

with $A = 170 \pm 40$ nm/V_{rms} the static response, $\omega_0/(2\pi) = 115.02 \pm 0.04$ Hz the resonance frequency and $Q = 66 \pm 2$ the quality factor. This first shows that the actuator response is linear in this entire frequency range, and is satisfactorily modelled by a harmonic oscillator. More importantly for the subject of this paper, this secondly shows that the signal analysis described here provides quantitative results. In particular, the corrections for the two types of non-linearities, due to optical and electronic imperfections and due to large amplitudes of harmonic oscillation, work whatever the frequency. We also find that the filtering condition given by equation 8 is fulfilled for frequencies as low as 10 Hz.

7. Discussion

Non-linearities due to optical and electronic imperfections. To our knowledge, the correction of the imperfections presented in section 4 have never been reported in the literature. More precisely, the amplitude ratio and phase shift between each pair of photodiodes, leading to periodic non-linearities when normalizing the photocurrents to compute the contrasts, have never been mentioned. One possible reason is that, in many cases, the signals are not normalized, perhaps because light source fluctuations have a negligible influence in these applications.

Generally, Heydemann corrections are applied off-line, i.e., after data acquisition, by digital analysis of the signals [19, 4, 3, 20], as we have done in the present

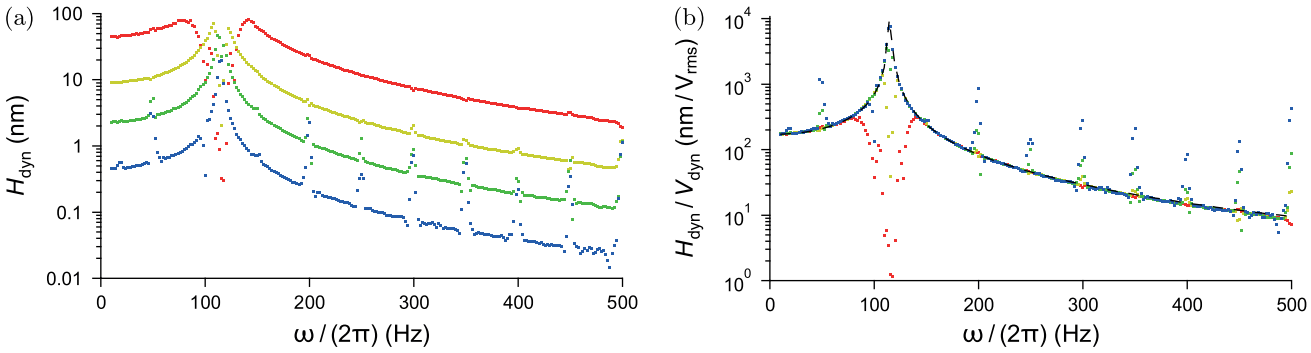

Figure 8. (**a**) Modulus of the harmonic displacement as a function of frequency, when applying a harmonic voltage of amplitude $V_{\mathrm{dyn}} = 0.0027$ $\mathrm{V_{rms}}$ (in blue), $V_{\mathrm{dyn}} = 0.013$ $\mathrm{V_{rms}}$ (in green), $V_{\mathrm{dyn}} = 0.053$ $\mathrm{V_{rms}}$ (in yellow) or $V_{\mathrm{dyn}} = 0.27$ $\mathrm{V_{rms}}$ (in red) to the actuator. (**b**) Same data, where the modulus of the harmonic displacement has been divided by the corresponding amplitude of harmonic voltage. The black dashed line is a fit with a harmonic oscillator model.

study. In order to achieve fast real time measurements, Heydemann corrections can also be applied live, i.e., prior to data acquisition, by electronic manipulation of the signals, with the ellipse parameters calibrated beforehand [21]; we believe that such approaches could be adapted to include the additional corrections presented here. Harmonic calibration has been shown to outperform the Heydemann corrections [22]. Such calibration may implicitly include the imperfections highlighted in this paper, but one of the advantages of our approach is that the imperfections and their origins are explicitly identified.

The use of optical shutters has proved to be an alternative method for calibrating the correction parameters when only a small part of the ellipse can be explored [23]. This method could also be implemented for our new corrections, except that it only works for ideal phase shifts (perfectly in-phase pairs of static signals, and perfect quadrature between X and Y channels), which presupposes perfect adjustment of the optical elements at the origin of these imperfections (Wollaston prisms, quarter-wave plate). The addition of another channel to simultaneously measure a fraction of the intensity coming from the light source has recently been proposed [24]. This could be done in our set-up, for example by adding a photodiode at the unused output of the first beamsplitter. Compensation for fluctuations in laser intensity could be achieved by normalizing the interference signals with this reference instead of combining each pair of signals, thus avoiding the non-linearities caused by the amplitude ratio and phase shift between them. Two-wavelength interferometry has proved suitable to correct periodic non-linearities [25], however such heterodyne techniques are much more complex to implement.

More generally, a wide variety of sophisticated optical interferometers have been designed -using two wavelengths, modulators, capacitive sensors, etc.- with exquisite sensitivity and linearity [26, 16], however a comparison of their performance with our implementation of quadrature phase interferometry is well beyond the scope of this paper, as it would require a dedicated review.

Non-linearities due to large amplitudes of harmonic oscillation. The corrections of the non-linearities presented in section 5 are only relevant in the case where the phase to be determined is the sum of a quasi-static component and a small harmonic component, with an analysis assuming that the harmonic component as a perturbation of the static one. Such a superposition probed by quadrature phase differential interferometry has, to our knowledge, mainly been tackled by our team in the context of the dSFA.

In a previous publication [15], we proposed a method to produce a single real-time analog output for quadrature phase interferometry. In short, it consisted in processing the total photocurrents (static plus harmonic) in home-made electronics to transform them into total contrasts as:

$$C^{\mathrm{X}} = \frac{I^{\mathrm{X1}} - I^{\mathrm{X2}}}{I^{\mathrm{X1}} + I^{\mathrm{X2}}} \tag{67}$$

$$C^{\mathrm{Y}} = \frac{I^{\mathrm{Y1}} - I^{\mathrm{Y2}}}{I^{\mathrm{Y1}} + I^{\mathrm{Y2}}}. \tag{68}$$

On one hand, these signals were sent to precision multimeters to obtain analog signals for the static contrasts ($C^{\mathrm{X}}_{\mathrm{stat}}$, $C^{\mathrm{Y}}_{\mathrm{stat}}$), which were numerically analysed to obtain the static phase and so the static displacement via Heydemann corrections. On the other hand, the total contrasts were sent in an electronic circuit performing the following operation [13]:

$$U = \left\langle C^{\mathrm{X}} \right\rangle \times C^{\mathrm{Y}} - \left\langle C^{\mathrm{Y}} \right\rangle \times C^{\mathrm{X}}, \tag{69}$$

which, under conditions of linearity, generates an analog signal that is simply proportional to the

harmonic phase and so to the harmonic displacement. In practice, periodic non-linearities were observed for the signal U as a function of the static phase, which were empirically calibrated with a truncated Fourier series.

Although this approach provides a single real-time analog output from a 4-channel interferometer for the harmonic displacement, it presents in this form several important limitations with respect to the imperfections reported in the present paper. First, particular care must be taken when installing this additional electronics to avoid inducing new imperfections as DC offsets, amplification errors and reduced bandwidth. Then, the amplitude ratio and phase shift between each pair of photodiodes were not taken into account for the electronic calculation of the contrasts. This lead to the observation of a trifolium for the residuals on the elliptical fit of the static contrast, and to periodic non-linearities in the determination of the static and harmonic displacements which were approximatively corrected with an empirical calibration. This could be resolved by correcting these imperfections electronically, in the spirit of the live Heydemann corrections that have been proposed previously [21]. There, the expansion for large amplitudes of harmonic oscillation was limited to order $n = 2$ with a coefficient which was determined experimentally, and the analysis neglected the effect on the static signals. Consequently, this analysis required an additional calibration, and it lead to even more pronounced periodic non-linearities in the determination of the static displacement and to a $\sim 10\%$ overestimation of the harmonic displacement. The analysis presented here, i.e., the expansion of the static and harmonic signals for large amplitudes of harmonic oscillation to an arbitrary order n, could be easily implemented to correct the non-linearities on the signal U, quantitatively and without specific calibration.

8. Conclusion

To summarize, this paper has dealt with two types of non-linearities that quadrature phase differential interferometry can suffer from. The first type of non-linearities is due to optical and electronic imperfections, specifically to amplitude ratio and phase shift between each pair of photodiodes. These imperfections have been clearly highlighted, their origins have been identified, and new calibrations and analysis have allowed to correct them. The second type of non-linearities is due to large amplitudes of harmonic oscillation. An analytical extension of the analysis to the non-linear regime of harmonic perturbation has been developed and successfully implemented. The methods proposed to correct the two types of non-linearities are very general and have proved effective over a wide range of quasi-static velocities, frequencies and amplitudes of harmonic oscillation.

We list below the key aspects of the new procedures of calibration and analysis.

- All the measurements should be carried out at sufficiently low quasi-static velocity (typically $v < 5$ nm/s for a red-emitting laser and a ~ 1 s sampling time) and with a sufficiently high frequency of harmonic oscillation (typically $\omega/(2\pi) > 10$ Hz for a ~ 100 ms integration time), to ensure the quasi-static, sampling and filtering conditions are met.
- Calibrations at constant constant quasi-static velocity and low amplitude of harmonic oscillation (typically $v \sim 1$ nm/s and $H_{\mathrm{dyn}} \sim 1$ nm) allow to precisely quantify the signals deviations from ideality due to optical and electronic imperfections. Eleven parameters, listed in Table 1, are extracted: 5 parameters are the usual ones introduced by Heydemann and obtained by elliptical fits, while 6 parameters are new and obtained by simple sinusoidal fits.
- Static and dynamic contrasts can be defined as in equations 42, 50 and 51 in order to correct all the non-linearities, except the ones due to phase shifts between each pair of photodiodes and to large amplitudes of harmonic oscillation.
- The phase shifts between each pair of photodiodes are small and can be corrected by determining the static phase iteratively (only ~ 3 iterations needed for a $\sim 1\%$ convergence).
- Large amplitudes of harmonic oscillation tend to reduce the amplitudes of the static and harmonic signals, by factors which can be calculated analytically from the harmonic phase to be determined. These effects can be taken into account quantitatively by determining the static and harmonic phases iteratively (only ~ 2 iterations needed for a $\sim 1\%$ convergence).

As shown in this manuscript, these non-linearities have a significant impact on the precision and accuracy of the measured displacements. Therefore, the correction of these non-linearities will be beneficial in a large number of applications of quadrature phase differential interferometry. It is particularly the case in the context of the dSFA [10], an instrument used in our team and for which this work was initiated. Its principle consists in confining a liquid between two solid surfaces, varying the distance between the surfaces and probing the force acting between the surfaces. The distance is controlled with a quasi-static component plus a dynamic component of sinusoidal

shape, and so does the force in the framework of the linear mechanical response of the system. Quadrature phase differential interferometry is then a tool of choice to measure these static and harmonic distance and force (via the deflection of an elastic element), typically ranging from 10 pm to 10 μm. The first type of non-linearities discussed here leads to periodic oscillations on the determined harmonic displacement, of $\sim 14\%$ in amplitude at the interferogram's period. The second type of non-linearities appears with large amplitudes of harmonic oscillation, which are often imposed to the distance between the surfaces in order to obtain a substantial, measurable, harmonic force. This leads to an underestimation of the harmonic displacement, all the more pronounced the greater the amplitude of harmonic oscillation, of $\sim 25\%$ for a typical oscillation of amplitude 70 nm. It is clear that all these errors should be avoided for the realization of quantitative measurements of the nano-rheology of confined liquids, and in particular for the fine and unambiguous determination of the hydrodynamic boundary condition, the so-called hydrodynamic slip length [11]. Finally, the correction of these non-linearities is important not only for the dSFA, but also for all mechanical studies requiring the measurement of nanometric displacements with an exquisite sensitivity. For example, the methods presented in this article might be of great interest for many applications including AFM [3], laser vibrometry [23, 27], or even the detection of protein folding [28].

Acknowledgements

This work was funded by Total and by the French National Research Agency through Grant No. ANR-19-CE30-0012. The authors thank Bruno Travers, Guillaume Donnier-Valentin and Thibaut Gandit for their help with electronic aspects.

References

[1] Nomarski G 1955 *J. Phys. Radium* **16** 9S–13S
[2] Schönenberger C and Alvarado S F 1989 *Rev. Sci. Instrum.* **60** 3131–3134 ISSN 0034-6748 URL https://doi.org/10.1063/1.1140543
[3] Paolino P, Aguilar Sandoval F A and Bellon L 2013 *Rev. Sci. Instrum.* **84** 095001 ISSN 0034-6748 URL https://doi.org/10.1063/1.4819743
[4] Bellon L, Ciliberto S, Boubaker H and Guyon L 2002 *Opt. Commun.* **207** 49–56 ISSN 0030-4018 URL https://www.sciencedirect.com/science/article/pii/S003040180201475X
[5] Sheppard C J R and Kou S S 2010 *AIP Conf. Proc.* **1236** 65–69 ISSN 0094-243X URL https://doi.org/10.1063/1.3426169
[6] Hernández-Montes M d S, Mendoza-Santoyo F, Flores Moreno M, de la Torre-Ibarra M, Silva Acosta L and Palacios-Ortega N 2020 *J. Eur. Opt. Soc.: Rapid Publ.* **16** 16 URL https://doi.org/10.1186/s41476-020-00133-8
[7] Javidi B, Carnicer A, Anand A, Barbastathis G, Chen W, Ferraro P, Goodman J W, Horisaki R, Khare K, Kujawinska M, Leitgeb R A, Marquet P, Nomura T, Ozcan A, Park Y, Pedrini G, Picart P, Rosen J, Saavedra G, Shaked N T, Stern A, Tajahuerce E, Tian L, Wetzstein G and Yamaguchi M 2021 *Opt. Express* **29** 35078–35118 URL https://opg.optica.org/oe/abstract.cfm?URI=oe-29-22-35078
[8] Yan L, Wang Q, Huang L, Chen B and Lin Y 2022 *Opt. Lasers Eng.* **148** 106780 ISSN 0143-8166 URL https://www.sciencedirect.com/science/article/pii/S0143816621002
[9] Marghany M 2024 *Oceanographic and Marine Environmental Studies around the Arabian Peninsula* 173
[10] Garcia L, Barraud C, Picard C, Giraud J, Charlaix E and Cross B 2016 *Rev. Sci. Instrum.* **87** 113906 ISSN 0034-6748 URL https://doi.org/10.1063/1.4967713
[11] Cottin-Bizonne C, Cross B, Steinberger A and Charlaix E 2005 *Phys. Rev. Lett.* **94**(5) 056102 URL https://link.aps.org/doi/10.1103/PhysRevLett.94.056102
[12] Heydemann P L M 1981 *Appl. Opt.* **20** 3382–3384 URL https://opg.optica.org/ao/abstract.cfm?URI=ao-20-19-3382
[13] Dandridge A, Tveten A and Giallorenzi T 1982 *IEEE Trans. Microw. Theory Techn.* **30** 1635–1641 URL https://doi.org/10.1109/TMTT.1982.1131302
[14] Smith S T, Chetwynd D G and Bowen D K 1987 *J. Phys. E: Sci. Instr.* **20** 977 URL https://dx.doi.org/10.1088/0022-3735/20/8/005
[15] Barraud C, Garcia L, Cross B and Charlaix E 2017 *Meas. Sci. Technol.* **28** 045103 URL https://dx.doi.org/10.1088/1361-6501/28/4/045103
[16] Watchi J, Cooper S, Ding B, Mow-Lowry C M and Collette C 2018 *Rev. Sci. Instrum.* **89** 121501 ISSN 0034-6748 URL https://doi.org/10.1063/1.5052042
[17] Abramowitz M and Stegum I A 1972 (National Bureau of Standards)
[18] Arfken G B, Weber H J and Harris F E 2013 (Elsevier Academic Press) ISBN 978-0-12-384654-9 URL https://doi.org/10.1016/C2009-0-30629-7
[19] Petru F and Cip O 1999 *Prec. Eng.* **23** 39–50 ISSN 0141-6359 URL https://doi.org/10.1016/S0141-6359(98)00023-3
[20] Dai G, Wolff H, Pohlenz F and Danzebrink H U 2009 *Rev. Sci. Instrum.* **80** 043702 ISSN 0034-6748 URL https://doi.org/10.1063/1.3109901
[21] Dai G, Pohlenz F, Danzebrink H U, Hasche K and Wilkening G 2004 *Meas. Sci. Technol.* **15** 444 URL https://dx.doi.org/10.1088/0957-0233/15/2/019
[22] Ferrero B and Bellon L 2022 *Europhys. Lett.* **139** 55002 URL https://dx.doi.org/10.1209/0295-5075/ac8761
[23] Zhu J, Hu P and Tan J 2015 *Appl. Opt.* **54** 10196–10199 URL https://opg.optica.org/ao/abstract.cfm?URI=ao-54-34-10196
[24] Bridges A, Yacoot A, Kissinger T and Tatam R P 2021 *Meas. Sci. Technol.* **33** 025201 URL https://dx.doi.org/10.1088/1361-6501/ac3aad
[25] Bridges A, Yacoot A, Kissinger T, Humphreys D A and Tatam R P 2021 *Meas. Sci. Technol.* **32** 125202 URL https://dx.doi.org/10.1088/1361-6501/ac1dfa
[26] Pisani M, Yacoot A, Balling P, Bancone N, Birlikseven C, Çelik M, Flügge J, Hamid R, Köchert P, Kren P, Kuetgens U, Lassila A, Picotto G B, Şahin E, Seppä J, Tedaldi M and Weichert C 2012 *Metrologia* **49** 455 URL https://dx.doi.org/10.1088/0026-1394/49/4/455
[27] O'Donoughue P, Gautier F, Meteyer E, Durand-Texte T, Secail-Geraud M, Foucart F, Robin O, Berry A, Melon M, Pézerat C, Pelat A and Picart P 2023 *Sci. Rep.* **13**(4) ISSN 2045-2322 URL https://doi.org/10.1038/s41598-023-30053-9
[28] Muñoz R, Aguilar-Sandoval F, Bellon L and Melo F 2017 *PLOS ONE* **12** 1–14 URL

https://doi.org/10.1371/journal.pone.0189979